Case Studies in Thermal Engineering 57 (2024) 104331

Contents lists available at ScienceDirect

Case Studies in Thermal Engineering

journal homepage: www.elsevier.com/locate/csite

Multimodal machine learning for predicting heat transfer characteristics in micro-pin fin heat sinks

Haeun Lee[a], Geonhee Lee[a], Kiwan Kim[a], Daeyoung Kong[b], Hyoungsoon Lee[a,c,1,*]

[a] *Department of Intelligent Energy and Industry, Chung-Ang University, Seoul, 06974, South Korea*
[b] *Department of Mechanical Engineering, Stanford University, Stanford, CA, 94305, USA*
[c] *School of Mechanical Engineering, Chung-Ang University, Seoul, 06974, South Korea*

ARTICLE INFO

Handling Editor: Huihe Qiu

Keywords:
Multimodal
Deep learning
Thermal management
Boiling
Two-phase flow
Micro-pin fin heat sink

ABSTRACT

As three-dimensional integrated circuit (3D-IC) chip technology advances, thermal management has become increasingly important because of increasing heat flux from thermal stacking. Micro-pin fin-embedded cooling has emerged as a promising solution for 3D-ICs, offering better thermal and hydraulic performance than conventional microchannel heat sinks. It is also easy to integrate into existing 3D-IC structures, such as through-silicon vias between stacks. The utilization of two-phase flow in micro-pin fins further enhances temperature uniformity and improves the heat transfer coefficient by leveraging latent heat. Nevertheless, predicting thermal performance in micro-pin fin heat sinks under boiling conditions remains challenging owing to intricate geometric shapes and diverse operating conditions. The present lack of correlation or theoretical models poses a significant obstacle. To address this problem, our study employed a Multimodal machine-learning (ML) approach, combining image data capturing boiling patterns of two-phase flow and information about geometric shape and operating conditions, to predict heat transfer characteristics in micro-pin fin heat sinks. We utilized experimental data comprising 155 types of boiling heat transfer data with the dielectric fluid FC-72 in two micro-fin shapes directly etched on Si. Four ML algorithms (XGBoost, LightGBM, Multilayer perceptron (MLP), and Multimodal ML) were employed to predict thermal performance. The correlation coefficient analysis before learning revealed the influence of each type of measurement data on the heater surface temperature during two-phase flow. Prediction accuracy was measured using mean absolute percent error (MAPE), and the results were compared in terms of maximum and average temperature depending on the characteristics of each ML algorithm. Overall, the Multimodal approach demonstrated superior capability in predicting temperature distributions with spatial details, surpassing conventional decision-tree algorithms and MLP in performance. When trained with boiling images, the Multimodal ML model achieved remarkable precision, evidenced by a MAPE of 1.81% for the maximum temperature and 0.84% for the average temperature, highlighting its exceptional accuracy in mapping the heated surface temperature profile. By contrast, the traditional MLP model, which lacked training on boiling images, showed diminished accuracy, with a MAPE of 2.54% for the maximum temperature and 1.77% for the average temperature, indicating a comparative shortfall against the Multimodal model results.

* Corresponding author. School of Mechanical Engineering, Chung-Ang University, Seoul, 06974, South Korea.
E-mail address: leeh@cau.ac.kr (H. Lee).
[1] Website: http://atsla.cau.ac.kr

https://doi.org/10.1016/j.csite.2024.104331
Received 5 August 2023; Received in revised form 17 March 2024; Accepted 30 March 2024
Available online 31 March 2024

Nomenclature

A	area [m^2]
C_p	specific heat [J/kg·K]
D_f	pin fin diameter [mm]
h	enthalpy [J]
h_{conv}	heat transfer coefficient [W/(m^2·K)]

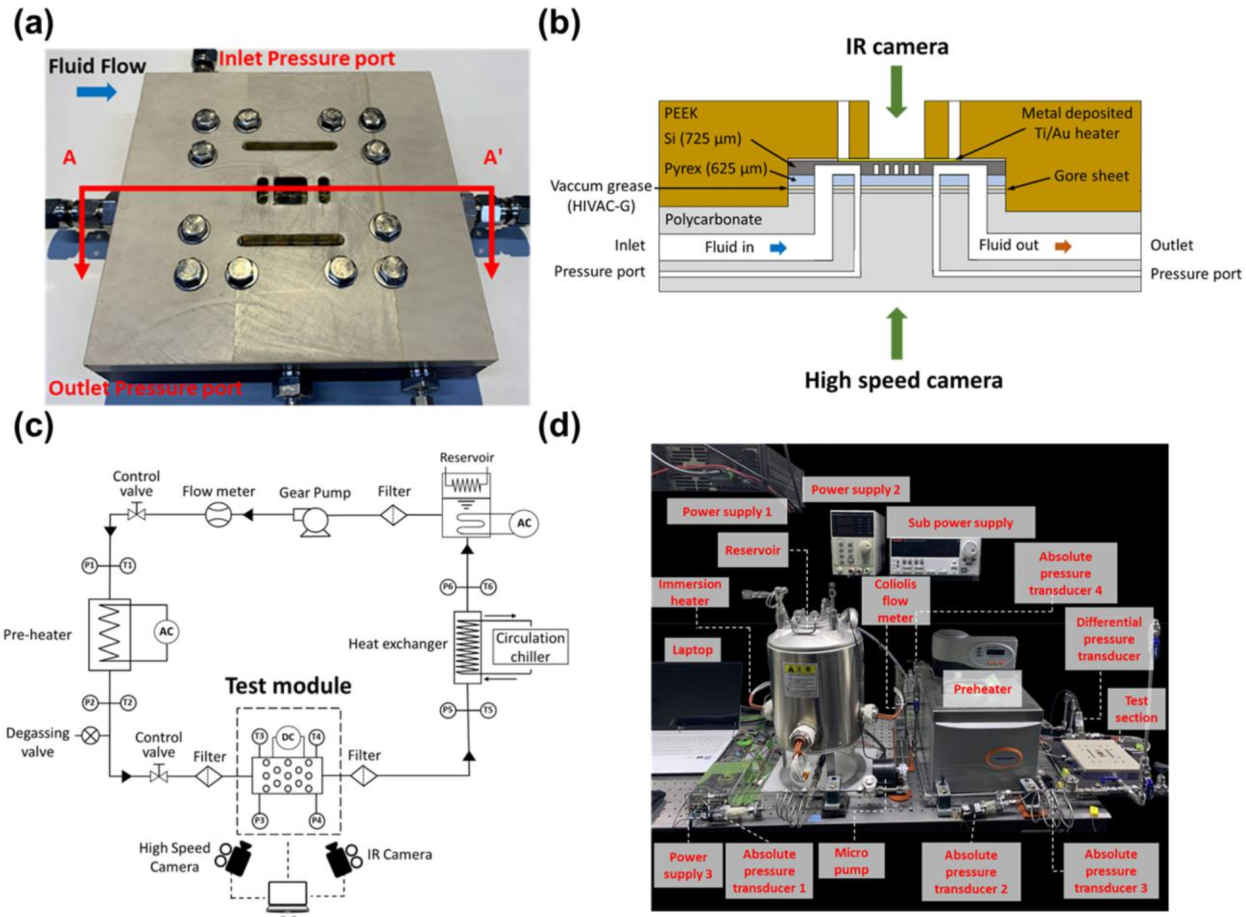

Fig. 1. Experimental setup and test section. (a) Photograph of the assembled test module, (b) Cross-sectional side view of the test module, (c) Schematic configuration of the flow loop, and (d) Photo of the equipment in the flow loop.

Table 1
Summary of a geometrical parameter value of the test sample and operating condition range in experiments.

Geometrical parameters and operating conditions	Case1: S_T = 200 [μm]	Case2: S_T = 300 [μm]
D_f [μm]	38.1	38.1
H_f [μm]	90.0	90.0
S_L [μm]	301	302
S_t [μm]	301	198
Arrangement	Staggered	Staggered
Shape	Circular	Circular
N_{row}	34	50
N_{column}	34	34
Mass flow rate [kg/s]	21.2–100.3	19.9–101.9
Heat flux [W/cm^2]	15.50–111.10	23.26–100.40
Inlet temperature [°C]	19.66–23.32	20.51–22.22
Pressure drop [kPa]	2.37–28.03	4.27–28.18
Heated surface temperature [°C]	63.5–121.5	74.6–138.0

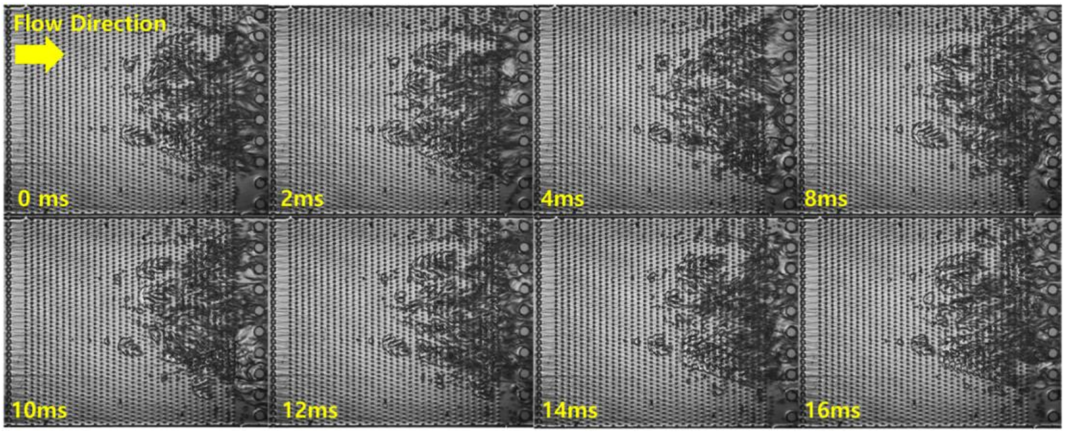

Fig. 2. Sequential high-speed images acquired during thermal tests. Specific test conditions of S_T = 200 μm sample under a mass flow rate 20 g/min and heat flux of 25 W/cm^2: each image captured at 100 fps (interval: 100/5000 s).

H_{fin}	pin fin height [mm]
k	thermal conductivity [W/m·K]
$\dot{m}$	mass flow rate [kg/s]
Nu	Nusselt number [−]
ΔP	pressure drop [kPa]
Pr	Prandtl number [−]
q	heat transfer rate [W]
q''	heat flux [W/m^2]
R''	total thermal resistance [K·cm^2/W]
Re	Reynolds number [−]
S_L	longitudinal pin fin spacing [m]
S_T	transversal pin fin spacing [m]
T_f	fluid temperature [K]
T_h	heated surface temperature [K]
u	fluid velocity [m/s]
V	voltage [V]

Greek symbols

ρ	density
μ	viscosity
σ	surface tension

Subscripts

avg	average
CFD	computational fluidic dynamics
exp	experiment
f	fluid
h	heater
in	inlet
min	minimum
max	maximum
pred	prediction
tot	total

1. Introduction

With the evolution of semiconductor process technology to meet market demands for improved performance, device miniaturization, and integration, the heat flux in electronic devices has continued to rise. Consequently, the maximum operating temperature has increased, leading to mechanical damage to connecting wires and solder due to differing thermal expansion coefficients [1]. Additionally, higher temperatures cause increased resistance, resulting in greater electrical losses and circuit performance deterioration, triggering severe electronic reliability issues and thermal failures [2]. Researchers have explored various thermal management techniques to address the challenge of high heat generation in electronic devices. These techniques include cooling methods using mi-

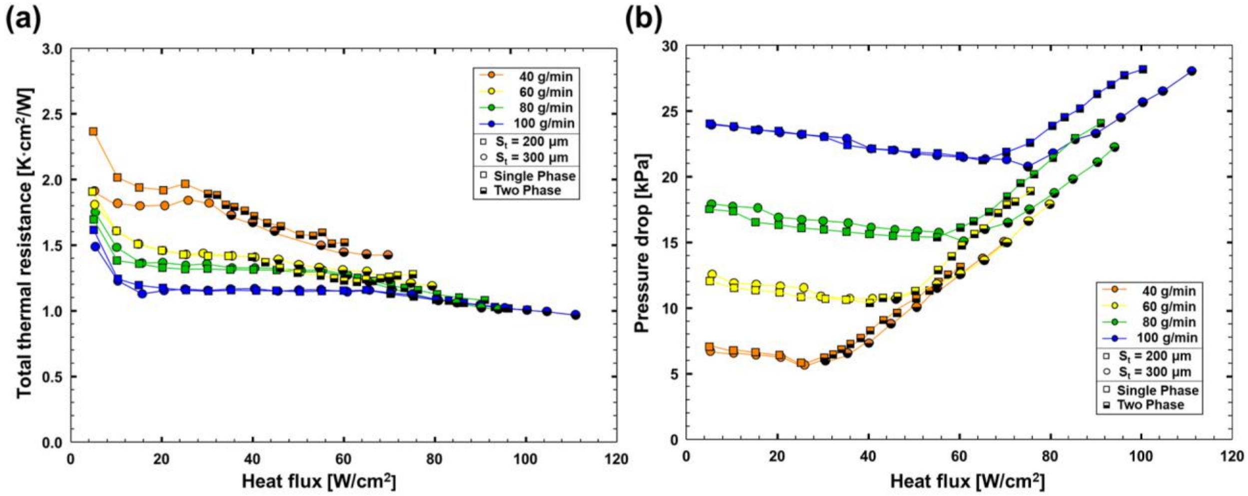

Fig. 3. Thermal and hydraulic performance of micro-pin fin heat sinks. (a) Experimental total thermal resistance as a function of effective heat flux. (b) Experimental pressure drop as a function of effective heat flux with mass flow rate.

crochannels [3], micro-pin fins [4], manifold microchannel structures [5], pool boiling [6], electrostatic spray [7], and jet impingement [8].

Three-dimensional integrated circuits (3D-ICs) are designed for high integration, minimizing electronic leakage due to device miniaturization. Although through-silicon via (TSV) reduces chip connection length, enhancing processing speed and power efficiency, it increases chip temperature owing to thermal superposition among stacked chips. Micro-pin fins offer an effective solution to this thermal problem, as they can be integrated into existing TSVs of 3D-ICs. Therefore, researchers have explored an embedded cooling technique for high-heat-flux 3D-ICs to manage heat generation effectively by fabricating micro-pin fins around TSVs between stacked chips [9,10]. Micro-pin fins offer a significant advantage in embedded cooling over conventional microchannels, as they provide an increased heat-transfer area with reduced pressure loss. Unlike microchannels, which require a larger channel height to mitigate high-pressure loss and result in electrical signal delay, micro-pin fins address this issue by offering decreased pressure loss. For these reasons, there have been many studies on the thermal and hydraulic performance of micro-pin fin heat sinks. Initially, the focus was on single-phase region performance using water or nonconductive refrigerants owing to their ease of experimentation [11]. Subsequently, multiphase research aimed to improve temperature uniformity in electronic devices while maintaining high heat-transfer performance at low flow rates [12]. However, experimental thermal performance measurements for two-phase flow in micro-pin fins are challenging and time-consuming, prompting thermal engineers to develop thermal performance correlations instead. Koşar and Peles [13] conducted an experiment in the multiphase region in the mass flux and heat flux ranges of 976–2349 kg/m^{2}s and 19–312 W/cm^2, respectively, using R-123 as the working fluid in the pinned fin structure. On the basis of experimental data, an empirical correlation with a mean absolute error (MAE) accuracy of 5% was developed to predict the Nusselt number of the exponential relationship to the Reynolds number (*Re*). Reeser et al. [14] conducted experiments in the mass flux and heat flux ranges of 200–1300 kg/m^{2}s and 1–118 W/cm^2, respectively, using water and HFE-7200 as working fluids. An MAE of 10.18% was recorded by a created correlation to predict the heat transfer coefficient using the exit quality and pressure drop from the experimental data. Krishnamurthy and Peles [15] compared the correlation equations for calculating various heat transfer coefficients using experimental data in the mass flux and heat flux ranges of 346–794 kg/m^{2}s and 20–350 W/cm^2, respectively, using water as the working fluid. The correlation equation of Kawahara et al. [16], which introduced the Prandtl number and friction multiplier, matched the experimental and predicted values most accurately within the range of 20%. Qu and Siu-ho [17] implemented square-shaped fin fins arranged in a staggered arrangement using water as the working fluid for mass flow rates of 183–420 kg/m^{2}s and heat fluxes in the range of 23.7–248.5 W/cm^2 at inlet temperatures of 30 °C, 60 °C, and 90 °C. On the basis of the heat transfer coefficient measured in the high-exit-quality region of the working fluid approaching the saturation temperature, a correction coefficient considering the reinforcing effect of subcooling was added to calculate the heat transfer coefficient in the multiphase region, and MAE accuracy of 7.6% was shown.

The advancement of computing devices and machine-learning (ML) techniques has led to an increasing focus on using ML for predicting thermal and hydraulic performance. The key advantage of ML lies in its ability to achieve high-accuracy predictions by analyzing data, particularly in systems where clear correlations are challenging to identify [18]. Consequently, active research is ongoing to apply ML in complex systems where parameter tendencies are difficult to determine by traditional experiments or computational fluid dynamics (CFD) methods. Qiu et al. [19] predicted the pressure drop in two-phase flow using an artificial neural network (ANN), XGBoost, LightGBM, and K-nearest neighbor algorithms in microchannels. All algorithms showed better prediction accuracies than conventional correlations, with the most accurate MAE of 9.58% in the ANN model. Yang et al. [20] derived five optimized features using single-phase flow CFD analysis data for 300 arbitrary spline-pin fin shapes using the pix2pix network and a genetic algorithm (GA). Lee et al. [21] performed learning of feature and operating condition data from 22 published papers on MLP ML models to predict universal friction factors applicable to micro-pin fin geometries, recording an accuracy of up to 14.49% MAE, more than 4.72

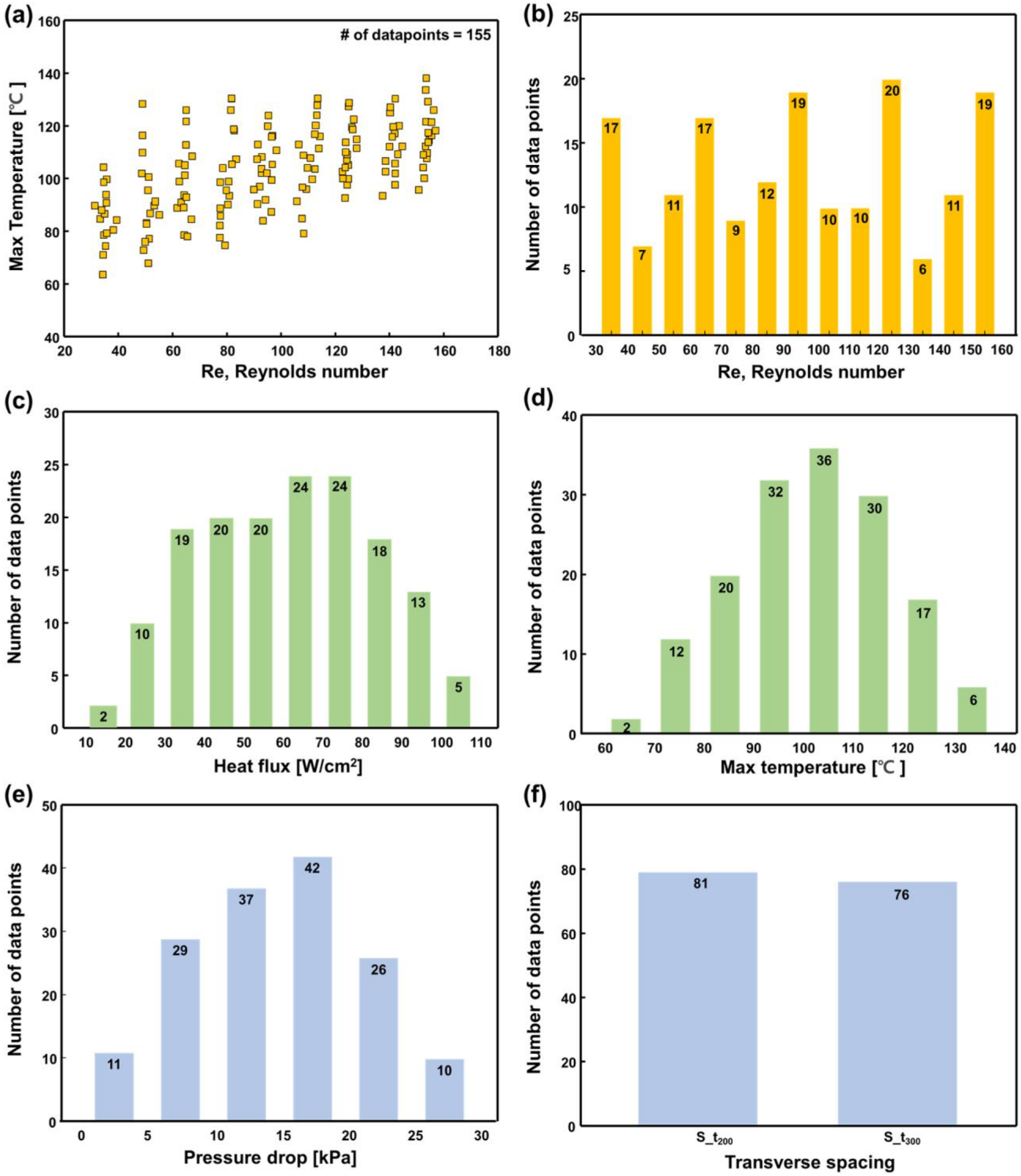

Fig. 4. Detailed dataset distribution for ML analysis. (a) Dataset in terms of maximum temperature versus Reynolds number. Dataset distribution with respect to (b) Reynolds number, (c) Heat flux, (d) Max temperature, (e) Pressure drop, and (f) Transverse spacing.

times higher than the existing power sum-based correlation [22]. Kim et al. [23] recorded a maximum MAE accuracy of 10.9% by learning the shape and operating condition data from 15 papers published in MLP, XGBoost, and LightGBM models for the universally applicable Nusselt number in the micro-pin fin. This was 2.17 times more accurate than the correlation formula created on the basis of the data. Suh et al. [24] automatically recognized bubbles generated during full boiling using convolution neural network (CNN)-based algorithms and then constructed a model to predict heat flux through bubble images using hierarchical and physical data to record a 6% mean absolute percent error (MAPE) accuracy. Nie et al. [25] made a prediction with 97.56% accuracy by constructing a

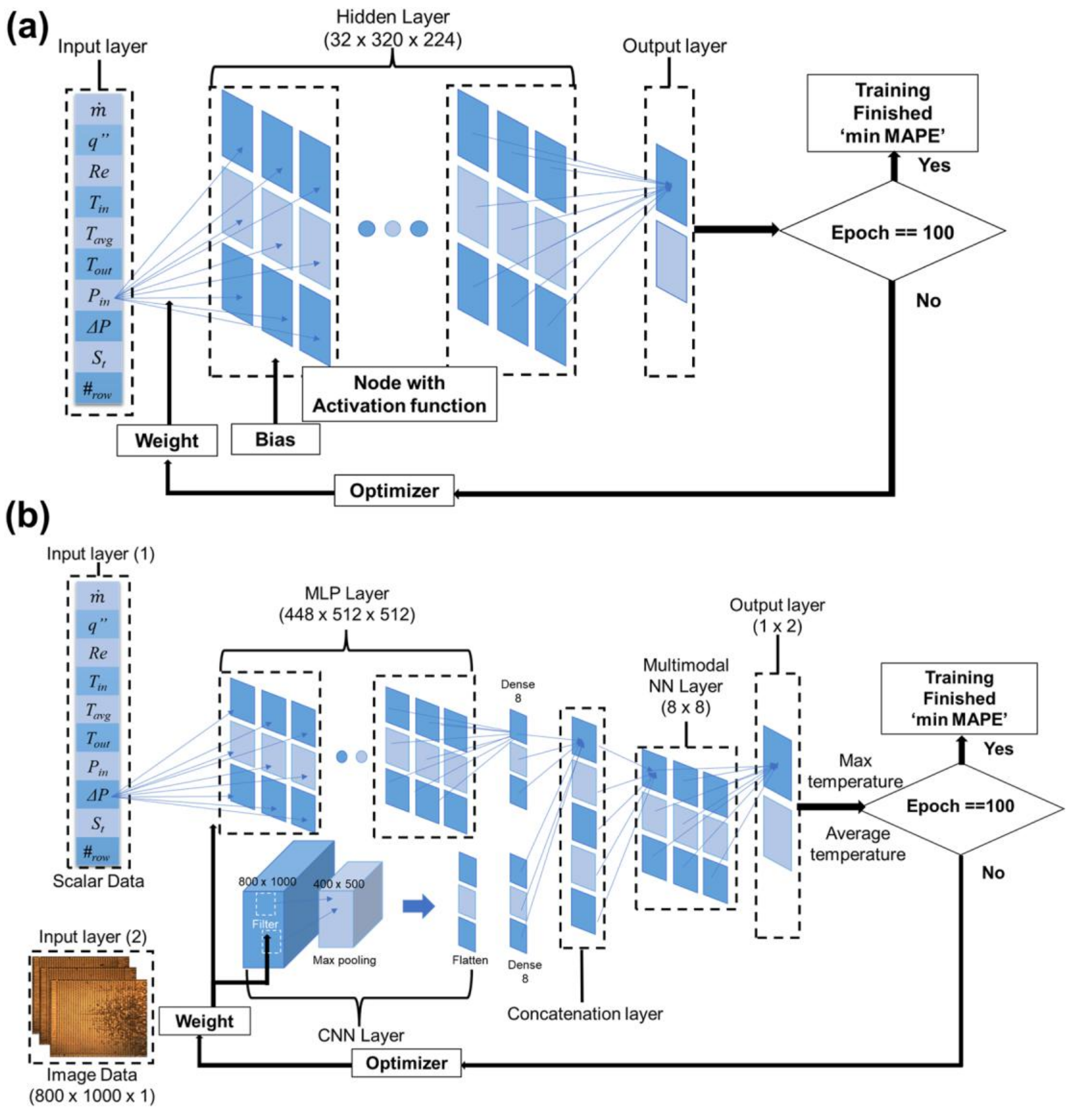

Fig. 5. Architecture of Algorithm. (a) Multilayer perceptron neural network, (b) Multimodal ML.

CNN-based algorithm to distinguish five flow patterns: tubular flow, bubble flow, stirring flow, slug flow, and hierarchical flow with 105,642 flow images under 696 conditions from horizontal circular tubes flowing methane and tetrafluoromethane. Zhang et al. [26] classified flow patterns in real time with 93% accuracy by performing learning of velocity information such as ultrasound doppler velocimetry, maximum speed, and maximum speed difference ratio in horizontal pipes in support vector machine, K-nearest neighbors, decision tree, long short-term memory, and CNN models.

As such, empirical correlations for predicting the performance of cooling systems in two-phase flow have limitations in terms of versatility due to the increased number of variables, compared to single-phase flow. Consequently, the accuracy of thermal performance predictions is significantly reduced. Specifically, compared to single-phase flow—which can be predicted solely on the basis of the geometric shape of cooling fins—flow boiling involves a larger number of variables and necessitates the use of time-varying image data to accurately predict the influence of flow patterns. In this research, we present a novel multimodal ML algorithm for predicting thermal performance in two-phase flow, utilizing both image and numerical data obtained from experimental micro-pin fin studies. We conduct a comparative analysis of the performance of our algorithm against other ML approaches that solely utilize numerical parameters. The proposed approach enables the accurate prediction of the thermal performance of heat sinks in two-phase flow, considering the influence of flow patterns and various parameters. The proposed modeling approach can provide contour-based temperature insights, identifying hot spots and their distributions within the chip. These capabilities offer a valuable resource for designs that integrate hot spot data, leading to enhanced operational efficiency and chip reliability by more accurate temperature predictions.

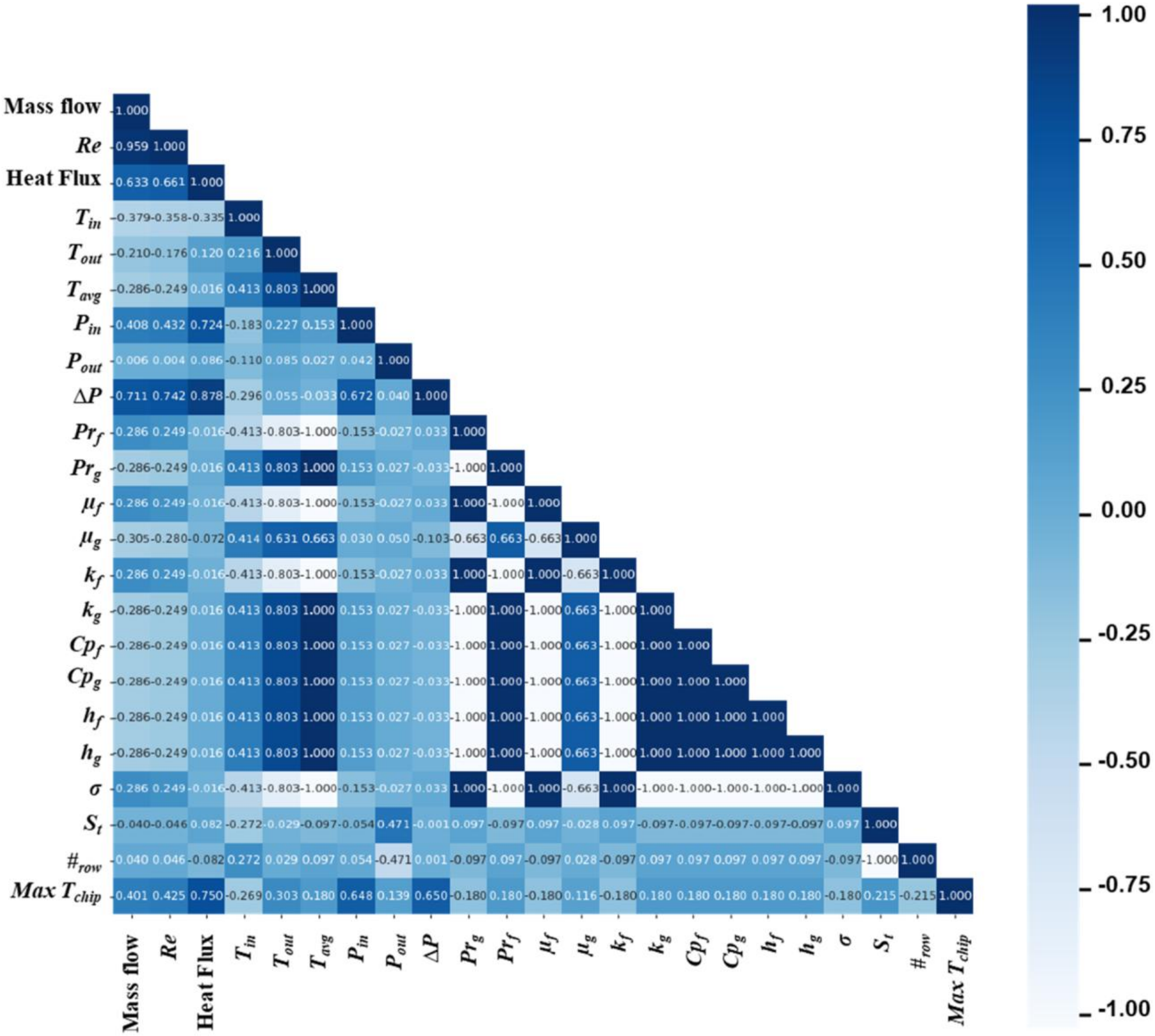

Fig. 6. Kendall rank coefficient heatmap for all variable scales between −1 to 1. All parameters exhibit a correlation coefficient with an absolute value of 0.1 or higher.

2. Methods

2.1. Experimental method

2.1.1. Experimental setup and measurement

We utilized FC-72 as the working fluid for conducting two-phase forced convection experiments on micro-pin fin samples. The detailed test vehicle fabrication process and loop configuration were identical to those in the previous study [27]. The micro-pin fin arrays were fabricated on a silicon wafer via a series of steps. Initially, a staggered micro-pin fin array (Circle, $D = 40$ μm, $S_T = 200$, 300 μm, and $S_L = 300$ μm) with pressure ports and an inlet orifice was etched onto the silicon wafer using a deep reactive ion etching process. Subsequently, a 500-nm-thick silicon dioxide (SiO_2) layer was deposited on the opposite side of the silicon substrate, followed by the application of a 200-nm-thick gold thin-film resistive heater. To enclose the fluid channel and enable optical flow visualization, the top side of the micro-pin fin array was covered with a Pyrex plate. Anodic bonding was employed to join the Pyrex cover and the silicon wafer by applying sequential voltages of 200 and 600 V at a temperature of 400 °C. Fig. 1(a) and (b) display the assembly and cross-sectional view of the test module, respectively. The test module, which comprised polycarbonate (Lexan) and polyether ether ketone slabs, facilitated the easy connection of fittings and electrical wiring while providing sufficient compression strength to prevent bursting during high-pressure tests. Fluid inlets and outlets were served by two 1/4″ Swagelok fittings, while temperature and pressure measurement ports were accommodated by two 1/16″ and two 1/8″ fittings, respectively. Fig. 1(c) and (d) respectively depict a schematic diagram and photograph of the actual equipment used in the experimental flow loop for thermal and hydraulic measurements. The flow circulation was achieved using a gear pump (Micropump GA-T23), and a flow meter (KIF510) was subse-

Table 2
Summary of an ML algorithm based on data modality, data size, and predicted temperature type.

Algorithm	Trained data modality	O/X	The number of Data	Predicted temperature type
XGBoost	Physical scalar	O	155	Scalar
	Image	X	–	
LightGBM	Physical scalar	O	155	Scalar
	Image	X	–	
MLP	Physical scalar	O	155 (for scalar& array)	Scalar and Contour
	Image	X	–	
Multimodal ML	Physical scalar	O	155 (for scalar)	Scalar and Contour
	Image	O	3100 (for contour)	

quently installed to measure the flow rate. The temperature of the heated area was captured by an infrared camera (FLIR E75) with a resolution of 320 × 240 pixels. The temperature change of the working fluid was monitored using K-type thermocouples at the inlet and outlet plenums of the sample, and pressure measurements were acquired using an absolute pressure measurement sensor (TRAFAG EPI8287) and a differential pressure transducer (Omega PX409) at the same locations. A titanium/gold (10/200 nm) thin-film resistive heater powered by a DC power supply (Keysight 6030A) was employed to provide heat to the heated surface. The power input to the heater was measured by a voltage divider comprising two resistors of 47 kΩ ± 0.1% and 3 kΩ ± 0.1% and a shunt resistor of 0.05 Ω ± 0.5%. Flow rate, inlet/outlet fluid pressure and temperature, and the power applied to the heater were recorded using NI Compact DAQ and LabVIEW.

Each measurement was taken over a 60-s period after the pressure, temperature, and heated surface temperature of the inlet/outlet fluid stabilized within ±0.3 °C. Following this, the flow rate was increased incrementally by 10 g/min, and the supply power was adjusted upwards by 3 or 5 W for different experimental runs, a process that was systematically repeated. The surface temperature of the heater was measured using an infrared (IR) camera with an accuracy of ±2%, while a K-type thermocouple provided a fluid temperature measurement with an accuracy of ±0.4%. The pressure measurements at the test site were accurate to within ±0.5%. Power to the heater, supplied by a DC power source, was controlled with an accuracy of ±0.3 W. The overall uncertainty in thermal resistance, which ranged from 0.02% to 0.1%, was calculated by applying error propagation techniques [28] to consider the uncertainties in the temperature of the heater measured by the IR camera, the temperature of the fluid measured by the thermocouple, and the heat flux measured by the power supply.

2.1.2. Compiling datasets from the experiment

We utilized two designs of samples to conduct experiments at various heat fluxes and mass flow rates. The experimental data included scalar-type measurements acquired from sensors and three-dimensional data from boiling images captured using a high-speed camera. In total, we conducted 155 experimental cases. These datasets were employed in our ML approach. The geometric shape values of the detailed samples and the ranges of the measured data are listed in Table 1.

Parameters from all 155 cases in the multiphase experiment were recorded at a sampling rate of 5 s^{-1} for a duration of 60 s, representing average values over time. Boiling images were captured using high-speed cameras at 5000 fps for 0.5 s^{-1}. The continuous images are shown in Fig. 2. Although the high-speed boiling images and measured physical values were not synchronized in time, we expanded the data by considering sets of 20 boiling images taken at 100-fps intervals as a group of image data in one case.

The measured physical data obtained from scalar-type measurements were considered constant as it was assumed to be in a steady state. This resulted in the multiplication of 155 cases of data into 3100 data points, which were used in ML algorithms for both non-proliferated and proliferated datasets. The scalar-type data measured in each experimental case included heat flux (q''), mass flow rate ($\dot{m}$), inlet/outlet fluid temperature (T_{in}, T_{out}), pressure loss (P_{in}, P_{out}), Reynolds number (Re), the pitch of row pins, number of row pins, superfast images of changes in boiling patterns captured at 5000 fps, and temperature distribution (40 × 40 resolution) of heaters measured by the IR camera. The two samples had distinct geometric differences, specifically the pitch of the row direction pins (S_L) and the number of row direction pins (N_L). These two geometrical factors were utilized in the ML learning process to account for the geometrical differences between the samples. The definition of the Reynolds number and the total heat resistance of the cooler is as follows:

$$Re = \frac{\rho u_{\max} D_f}{\mu} \tag{1}$$

$$A_{min} = H_f W \left(1 - \frac{D_f}{S_T}\right) \tag{2}$$

$$u_{max} = \frac{\dot{m}}{\rho A_{min}} \tag{3}$$

$$R'' = \frac{T_{heater} - T_{f,in}}{q''} \tag{4}$$

In Eq. (1), ρ and μ represent the density and viscosity of the working fluid, respectively. The average values of these properties were employed at the inlet and outlet temperatures of the liquid. For $u_{\max}$, the value of the flow rate generated in the minimum area ($A_{\min}$)

Table 3
Optimal hyperparameters based on Bayesian optimization.

Algorithms	Hyperparameter	Value
MLP	Layer	3
	Node	448-512-512
	Activation function	LReLU – LReLU- LReLU
	Learning rate	0.076
XGBoost	Colsample bytree	0.5727
	Colsample bylevel	0.0
	Colsample bynode	0.5566
	gamma	0.0
	Learning rate	0.2574
	Max depth	364
	Min child weight	0
	N_estimators	8034
	Reg alpha	39
	Reg lambda	753
	Scale pos weight	0.1202
	Subsample	1.0
LightGBM	Bagging fraction	0.9289
	Colsample bytree	0.5176
	Feature fraction	0.2415
	Lambda_L1	0.3678
	Lambda_L2	0.3994
	Learning rate	0.3196
	Min child samples	3.8923
	Min child weight	4.2288
	Max depth	366
	N estimators	1010
	Num leaves	782

between the pins was used. D_f represents the diameter value of the pin, considering the shape of the circular pin as the hydraulic diameter. T_{heater} in Eq. (4) corresponds to the temperature of the thin-film heater; in this study, the maximum value of the heater was utilized to represent thermal resistance. The value of q'' was calculated by dividing the measured power by the area of the heater, which had a size of 10 mm × 10 mm.

Fig. 3 presents the data distribution in the consolidated database used for the ML model. Fig. 3(a) illustrates the total thermal resistance relative to the heat flux under two geometric conditions and across four flow rates. The total thermal resistance, calculated using Eq. (4), gradually decreases with increasing heat flux at all flow rates. This trend continues until the onset of nucleate boiling (ONB) point is reached, at which point multiphase flow initiates, significantly enhancing cooling performance. An increase in the flow rate reduces the heater temperature for a given heat flux, leading to enhanced convective heat transfer and a reduction in total thermal resistance. Fig. 3(b) depicts the pressure drop as a function of heat flux, showing that higher mass flow rates result in larger pressure drops. It is also evident that an increase in heat input reduces the pressure drop in the single-phase region, while beyond the ONB point, there is a significant and sharp increase in pressure drop. Moreover, Fig. 3(a) indicates that under the same mass flow rates and heat flux, the difference in resistance for two micro-pin fin spacings of 200 and 300 μm is minimal, at approximately 5%. However, the pressure drop data presented in Fig. 3(b) reveal up to a 20% variation in performance according to the spacing, attributed to the acceleration and friction pressure drops in two-phase flow, which intensify with increased spacing density. Fig. 3(a) and (b) illustrate the data distribution in the ML model database, with all points corresponding to cases in the multiphase region immediately following the onset of boiling.

Fig. 4(a) displays the distribution of the maximum surface temperature with respect to the Reynolds number, obtained from Eq. (1). Fig. 4(b–f) present the data point distribution for the Reynolds number, heat flux, maximum surface temperature, pressure drop, and two distinct fin spacings. Furthermore, Table 1 provides the operating conditions and measurement ranges for all experimental parameters. Out of the total 155 data points, 10% were selected as test data, with the remaining 90% divided into training and validation sets in a 70%:30% ratio, respectively. This partitioning facilitated K-fold validation (5-fold) to mitigate dataset bias. The test data were intentionally chosen from diverse operating conditions to ensure a fair evaluation of the prediction performance.

2.2. Proposed ML model

We carefully selected all relevant factors related to the geometric shape and operational conditions as parameters for correlation analysis. Subsequently, we compared the accuracy of heated surface temperature prediction using the Multimodal ML approach, incorporating image data with flow patterns, with two different forms (scalars and contours) and four distinct ML algorithms. Fig. 5 illustrates a schematic diagram depicting the input layer, hidden layer, and output layer for MLP and Multimodal.

2.2.1. Selection of parameters

We performed Kendall-tau analysis to select the parameters for temperature prediction according to the experimental data features [29]. Fig. 6 presents the Kendall rank coefficient heatmap for the maximum heated surface temperature in each experimental

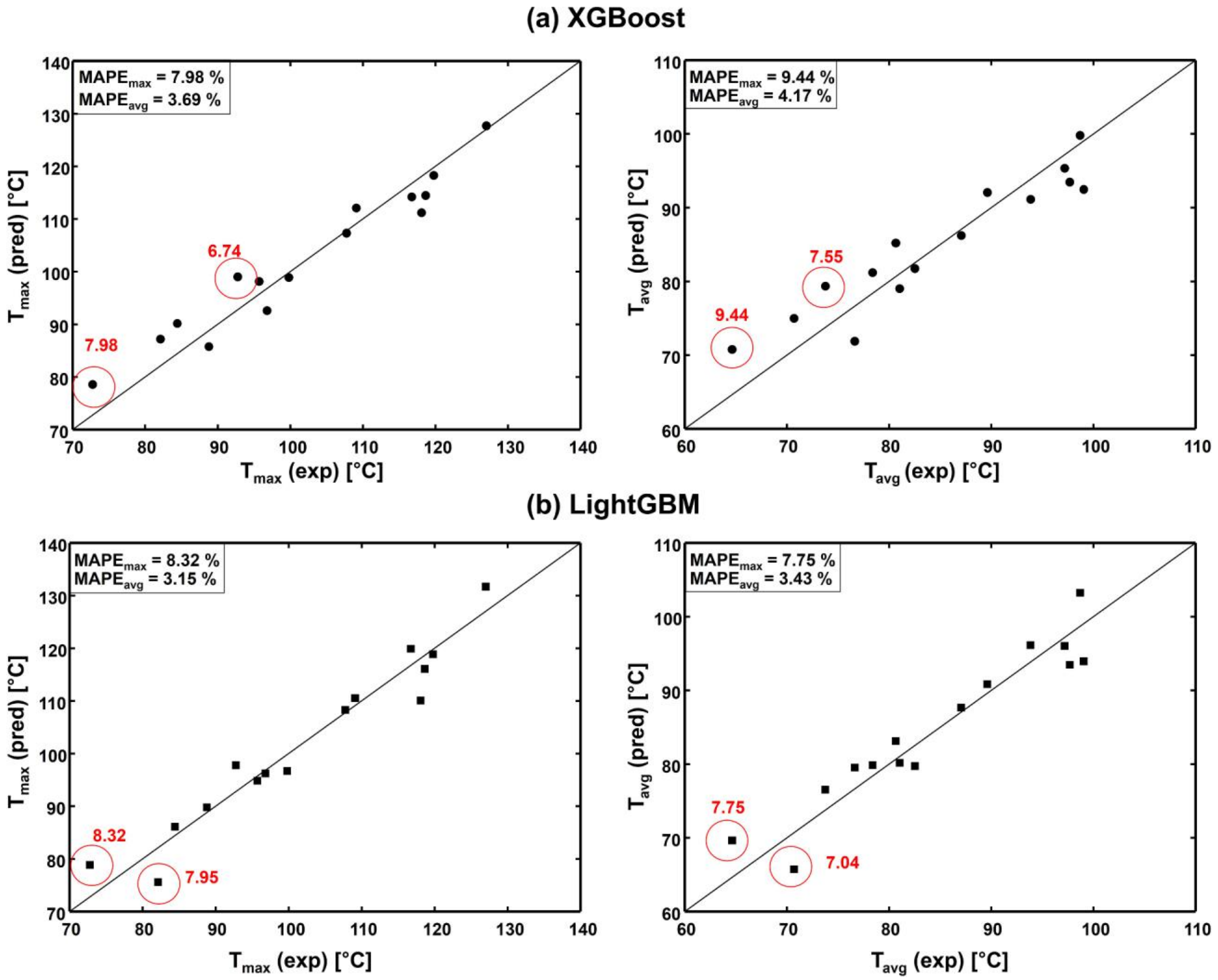

Fig. 7. Comparison of experimental and predicted scalar-form heated surface temperature. Predictive results using two specific ML algorithms: (a) XGBoost, (b) LightGBM.

case, indicating the extent of influence of each parameter on the maximum temperature. Kendall rank correlation is an effective non-parametric method for analyzing small datasets owing to its focus on relative order rather than specific values. Eq. (5) shows the Kendall rank correlation between variables x and y, where τ represents the Kendall rank coefficient ranging from −1 to +1. A value closer to +1 indicates a positive correlation with the variable, while a value closer to −1 indicates a stronger negative correlation. Utilizing this method, we analyzed the correlation coefficients of different parameters with the maximum heated surface temperature. In this analysis, the thermophysical properties of the parameters were extracted as per the average temperature of the fluid. Heat flux and pressure drop exhibited very high correlation coefficients with values of 0.75 and 0.65, respectively, with respect to the maximum surface temperature. By contrast, parameters related to fluid properties (*Pr, μ, k, Cp, h,* and σ) showed relatively lower correlation coefficients, with absolute values ranging from 0.12 to 0.18. However, all parameters exhibited a correlation coefficient with an absolute value of 0.1 or higher, indicating their relevance to the maximum heated temperature. Thus, all parameters were selected for ML analysis to ensure high-accuracy predictions.

$$\tau = \frac{2}{n(n-1)} \sum_{i<j} \operatorname{sgn}\left(x_i - x_j\right) \operatorname{sgn}\left(y_i - y_j\right) \tag{5}$$

2.2.2. XGBoost and LightGBM

XGBoost [30] and LightGBM [31] are gradient-boosting decision tree-based algorithms, which are ensemble-learning techniques that combine consecutive decision trees to create a highly accurate model. XGBoost uses classification and regression trees for learning [32], and it incorporates a regularization term in the objective function to prevent overfitting and improve speed by parallel processing. However, one drawback of XGBoost is its time-consuming learning process because it scans all data to obtain feature information. To address this issue, LightGBM was introduced, which enhances learning speed and accuracy by implementing gradient-based one-side sampling techniques. These techniques only use large gradient data for information gain, excluding data with small gradi-

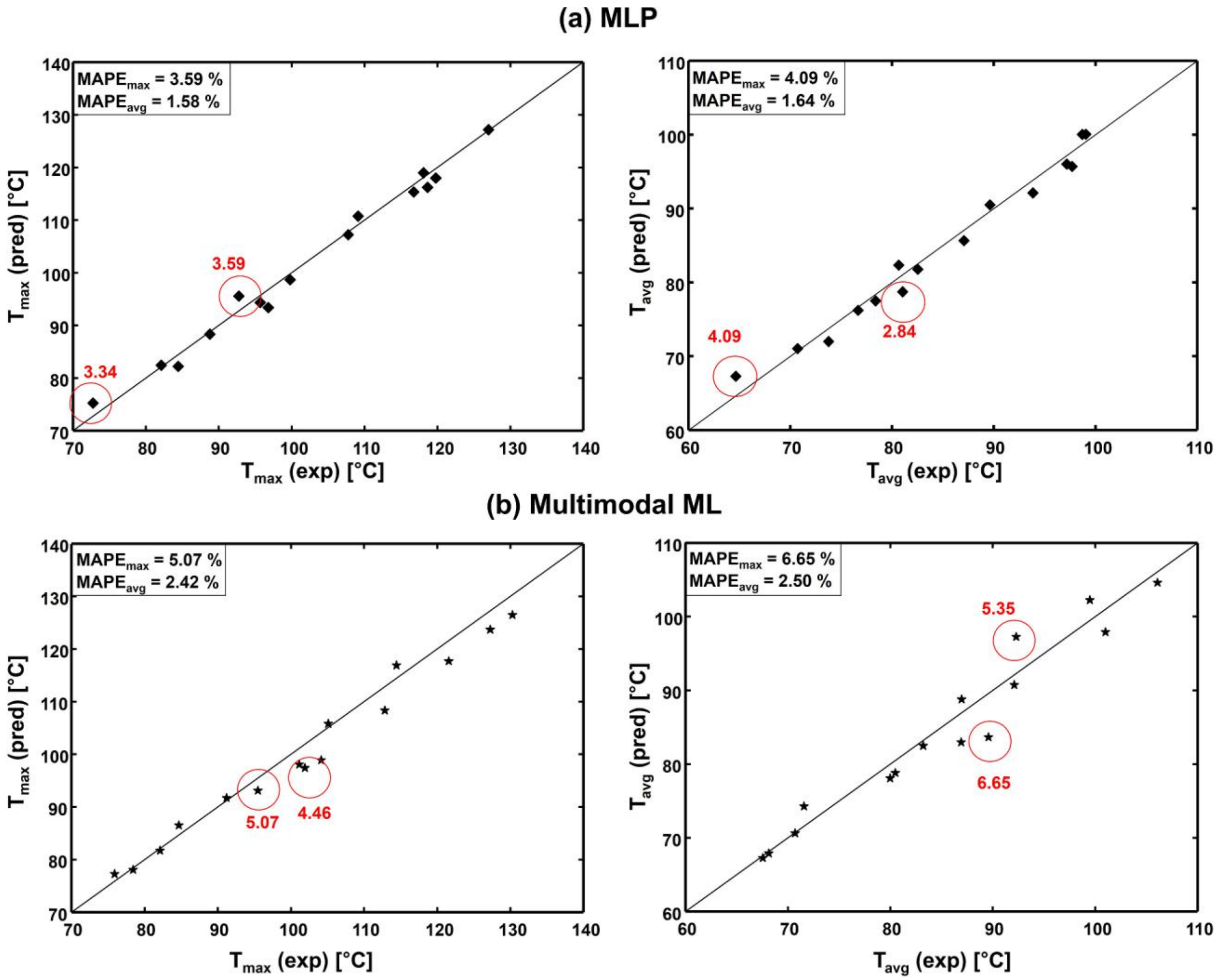

Fig. 8. Comparison of experimental and predictive results for scalar-form heated surface temperature. Predictions using two ML algorithms: (a) MLP, (b) Multimodal ML.

ents. Additionally, LightGBM employs exclusive feature bundling techniques to focus solely on important data features during learning [31]. In our study, we utilized the Multioutput regressor algorithm to predict the maximum and minimum values of temperature distributions in each experimental case. For the learning process, we used XGBoost's XGBRegressor (version 1.4.2) and LightGBM's LGBMRegressor (version 3.2.1).

2.2.3. MLP

MLP is a neural network technique that connects layers of perceptrons with weights and biases to form a multilayer structure, including an input layer, a hidden layer, and an output layer. Learning is achieved by updating the output value for each node using the activation function. In this study, a model was constructed using Python (version 3.9.9) and TensorFlow (version 2.4.0) for learning. Leaky rectified linear unit (LReLU) (alpha = 0.2) and hyperbolic tangent function were chosen as activation functions for comparing predicted values. The equations for each activation function are given by Eqs. (6) and (7). LReLU returns the same value if the input is positive and a value 0.2 times the input for negative values. The hyperbolic tangent function is advantageous for predicting nonlinear relationships, as it maps the input value to a value between −1 and 1 by an exponential relationship in the equation. The initial weights were initialized using the He method, and a fixed seed number was used to ensure the reproducibility of random selection values during learning. The output, which represents the predicted value, was updated using the Adam optimizer [33], which combines AdaGrad [34] and RMSprop [35].

$$f(x) = \begin{cases} x & \text{for } x \geq 0 \\ 0.2x & \text{for } x < 0 \end{cases} \tag{6}$$

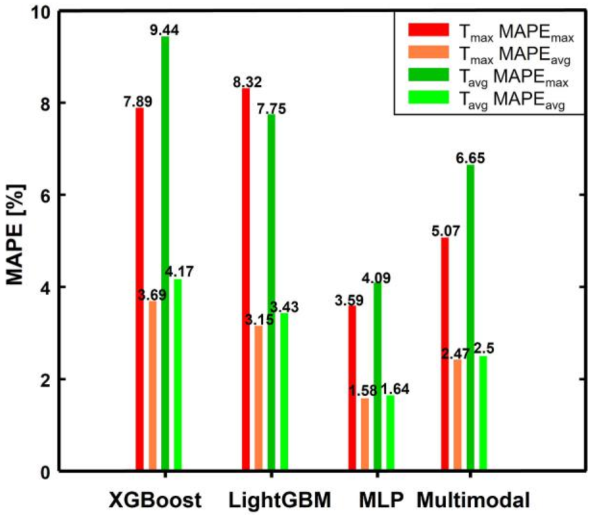

Fig. 9. Comparative summary of scalar temperature prediction accuracy achieved by each ML algorithm. MLP demonstrated the highest accuracy in predicting scalar temperature.

$$tanh(x) = \frac{e^x - e^{-x}}{e^x + e^{-x}} \tag{7}$$

2.2.4. Multimodal ML

In the context of ML, modality refers to the various ways or dimensions by which data is experienced or obtained [36]. Similar to how living organisms make judgments by processing comprehensive information obtained from different sensory organs, such as hearing, sight, and touch when detecting something, multimodal ML techniques utilize data from diverse sources or modalities for prediction. Multimodal ML can be categorized into three approaches:

1. Integrating data from different characteristic dimensions to make predictions.
2. Combining prediction values from different models with weights after learning with each model.
3. Using separate artificial neural networks to learn data from each modality, extracting embedded scalars, and then integrating these scalars for the final learning [37].

In our study, we adopted the third approach, integrating the previously optimized MLPNN and CNN models as a base. We constructed a Multimodal ML algorithm capable of outputting predictive values in desired formats, such as scalars and contours, by leveraging data from multiple modalities. (See details in Table 2).

2.3. Bayesian hyperparameter optimization

We performed hyperparameter optimization using Bayesian optimization to find the optimal hyperparameters that minimize the MAPE for each algorithm. Bayesian optimization was found to be the most efficient method in terms of time and cost savings for identifying the optimal values compared to other hyperparameter optimization techniques [38]. This approach recommends candidate hyperparameter values based on stochastic estimation using the acquisition function value at the confidence boundary, considering previously learned hyperparameters during the optimization process, and seeking the maximum value of the objective function.

Each MLP, XGBoost, and LightGBM was fine-tuned using Bayesian optimization for hyperparameter optimization; the resulting optimal hyperparameters are presented in Table 3. For the MLP model, we combined it with a CNN layer to predict temperature values in scalar form, leveraging both image and scalar data through a Multimodal ML algorithm. To select the CNN layer hyperparameters, we used Grid Search, exploring various configurations for the number of filters (ranging from 2 to 16), filter size (ranging from 3 × 3 to 5 × 5), and layer thickness (ranging from 1 to 3) to find the best combinations of hyperparameter values. The CNN layer exhibited the best accuracy with four filters, a filter size of (3 × 3), and a layer thickness of 1. A thinner layer resulted in fewer parameters to be learned, ultimately improving the prediction accuracy. In summary, the Multimodal learning approach combined the MLP with hyperparameters selected by Bayesian optimization and the CNN with hyperparameters determined using Grid Search optimization within a limited range [39].

3. Results and discussion

3.1. ML temperature scalar prediction result

Fig. 7 shows the scalar-form predictions of the heated surface temperature using XGBoost and LightGBM. These predictions were obtained from two decision tree-based models; the plot shows the largest MAPE value and average MAPE in the upper left corner, with the outlier having the largest MAPE highlighted by a red circle. As described in section 2.3.1, the LightGBM model, being the

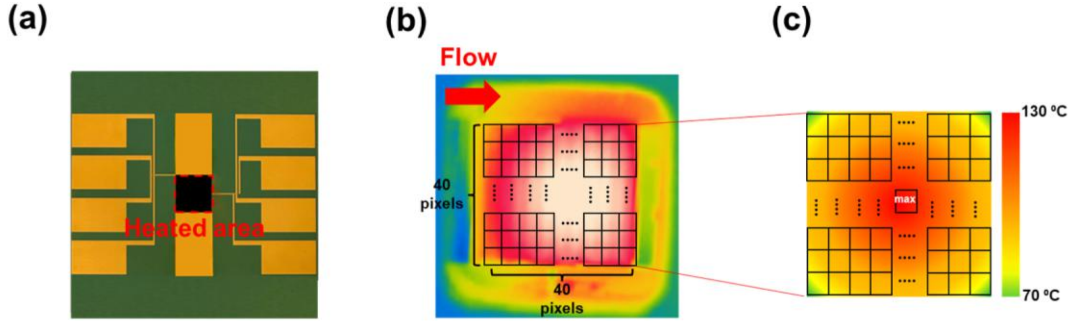

Fig. 10. Schematic of temperature distribution for contour-based heated surface temperature prediction. (a) Schematic of a gold thin-film-coated (200 nm) resistive heater, (b) Temperature distribution of the total section by flow direction, and (c) Temperature distribution of the heated section.

same decision tree-based prediction model as XGBoost, has shown improved accuracy in predicting both maximum and average temperature values in scalar form. The results for XGBoost and LightGBM indicated predictive accuracies of 3.69% and 3.15%, respectively, for maximum temperature, with an average MAPE, $MAPE_{avg}$, for the overall test data. The maximum MAPE, $MAPE_{max}$, for XGBoost and LightGBM was 7.98% and 8.32%, respectively. Similarly, for the average temperature value, the average $MAPE_{avg}$ was 4.17% for XGBoost and 3.43% for LightGBM, while the maximum $MAPE_{max}$ was 9.44% for XGBoost and 7.75% for LightGBM. Notably, both models showed higher MAPE values in areas with low temperatures. Out of the 155 data cases, only 14 data points fell within the relatively low-temperature region (60°C-80 °C), which accounted for less than 10% of the total dataset. Consequently, both models may have been slightly biased toward learning data from the relatively high-temperature region, and this was reflected in the results. Moreover, the characteristics of MAPE, which can yield high values even for minor differences in errors in small values, may explain why relatively large MAPE values appeared in the low-temperature region.

Fig. 8 shows the results of heated surface temperature prediction in scalar form using two approaches: MLP and Multimodal ML. We conducted a comparative analysis of the predictive accuracy for heated surface temperature between the MLP model, which was exclusively trained on scalar data, and the Multimodal ML model, which incorporated both scalar data and image data representing boiling characteristics [36]. The MLP model was utilized to learn and evaluate data solely in the same scalar form as the previous XGBoost and LightGBM models. The predicted results exhibited $MAPE_{max}$ of 3.59% and $MAPE_{avg}$ of 1.58% at the maximum temperature, as well as $MAPE_{max}$ of 4.09% and $MAPE_{avg}$ of 1.64% at the average temperature. By contrast, the Multimodal ML model demonstrated lower accuracy compared to MLP, which exhibited the highest accuracy. The prediction of the Multimodal ML model revealed a $MAPE_{max}$ of 5.07% and $MAPE_{avg}$ of 2.42% at the maximum temperature, as well as a $MAPE_{max}$ of 6.65% and $MAPE_{avg}$ of 2.50% at the average temperature. The difference in accuracy is likely due to the insignificance of the spatial information temperature in Multimodal ML when predicting the maximum and average temperatures in scalar form. Furthermore, among the four ML models used, only Multimodal ML exhibited high MAPE in the intermediate temperature range, while the other three models had high MAPE values in the low-temperature range. Additionally, when learning embedded scalars from data with varying characteristic dimensions using separate ANNs, it was determined that the increased learning features led to overfitting of the training data, resulting in lower accuracy than that of the MLP model. Fig. 9 presents a summary of temperature prediction MAPE in scalar form for the four previous ML algorithms. Remarkably, MLP exhibited superior performance compared to XGBoost, LightGBM, and Multimodal across all result forms. Consequently, temperature prediction in the contour form was conducted to incorporate spatial information on temperature and overcome the associated side effects.

3.2. ML temperature contour prediction result

Fig. 10 illustrates the temperature distribution schematic when predicting the heated surface temperature in contour form using different ML models. Fig. 10(a) shows the schematic of a gold thin-film-coated heater, which is of a serpentine type and operates via Joule heating. The periphery experiences the lowest temperature due to heat conduction and environmental heat loss to the surroundings. The central area forms a hot spot, attaining the maximum temperature owing to increased heat dissipation in this region. Because the heater operates at a constant voltage, the resistance at locations with higher temperatures increases, leading to additional heat dissipation. This phenomenon mirrors the occurrence of hot spots around the gate in actual semiconductor components, aligning with the phenomena observed when localized hot spots occur in real devices. Additionally, in the multiphase region, the highest temperature is observed near the ONB point, as the heated surface temperature decreases along the flow direction because of the pressure drop and corresponding decrease in saturation temperature. Fig. 10(b) and (c) present the results of the heater temperature distribution, reflecting these heater characteristics and multiphase flow characteristics.

Here, we solely utilized experimental cases containing the multiphase region in the data for the learning process, which allowed us to observe the same characteristics as the heated surface temperature distribution in the two-phase flow scenario. The temperature distribution of the 155 cases was represented as a 40 × 40 pixel contour, corresponding to the maximum resolution of the IR camera. Learning was conducted by utilizing this contour representation as the heated surface temperature label for each experimental case. The fundamental model used for learning was identical to the one employed for predicting the scalar form; however, the number of output nodes increased from 2 (used for predicting scalars) to 1600 (used for predicting contours). The performance was then compared by modifying the nodes just before the output layer.

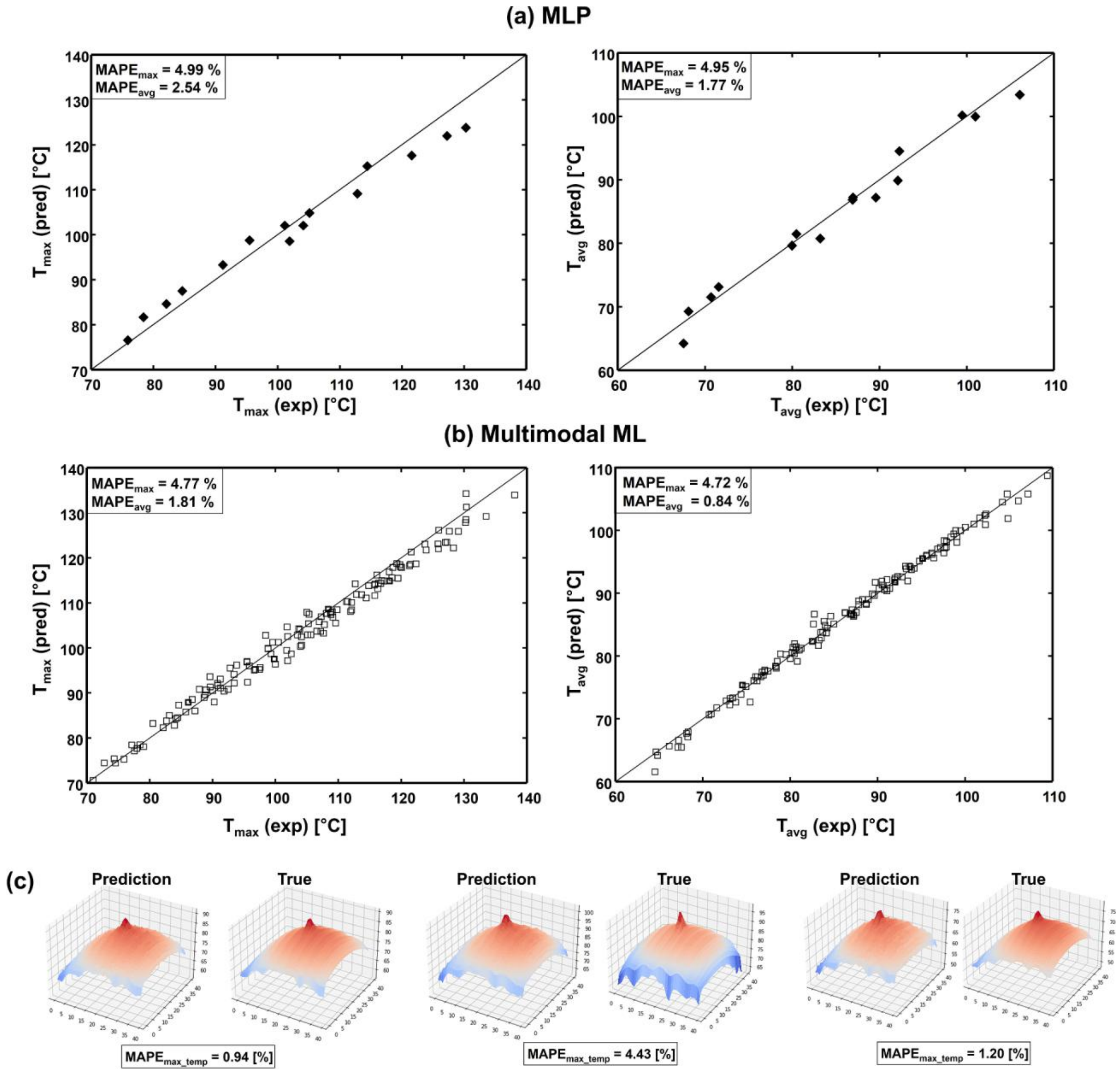

Fig. 11. Comparative analysis of heated surface temperature contour using ML predictive models. (a) MLP Prediction, (b) Multimodal ML prediction, and (c) Three example cases of the Multimodal ML-predicted contour compared to the true contour.

We performed heated surface temperature contour prediction using the MLP and Multimodal ML algorithms, excluding XGBoost and LightGBM, as they are based on decision trees and cannot predict the temperature distribution in contour form. For the MLP approach, we conducted learning with 155 experimental cases without utilizing continuous image data. However, Multimodal ML employed 3100 datasets that duplicated the same scalar data in experimental cases along with 20 consecutive images. In the case of Multimodal ML, the same temperature label was used for 20 consecutive datasets per case. The prediction accuracy of the learning results is illustrated in Fig. 11. The maximum and average values were extracted from the predicted temperature contour and compared. Interestingly, MLP showed lower accuracy in predicting the temperature distribution of the contour type compared to predicting the temperature in scalar form, with MAPE$_{max}$ 4.99% and MAPE$_{avg}$ 2.52% for the maximum temperature and MAPE$_{max}$ 4.95% and MAPE$_{avg}$ 1.77% for the average temperature.

Subsequently, when predicting the temperature distribution, the Multimodal ML approach demonstrated an accuracy of MAPE$_{max}$ 4.77% and MAPE$_{avg}$ 1.81% for the maximum temperature along with MAPE$_{max}$ 4.72% and MAPE$_{avg}$ 0.84% for the average temperature. Notably, these results displayed the lowest mean MAPE$_{avg}$ compared to the earlier predictions in scalar form, despite the number of values predicted being 800 times higher than in the scalar case.

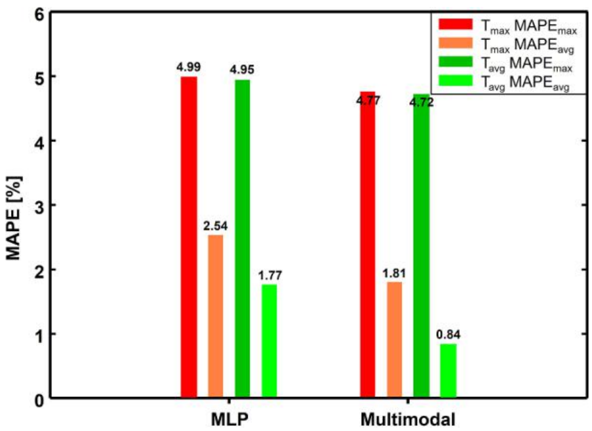

Fig. 12. Comparative summary of the contour temperature prediction accuracy of ML algorithms. The Multimodal ML model, incorporating image data, demonstrated superior accuracy compared to the traditional MLP model for average and maximum temperature predictions.

Furthermore, when predicting the heated surface temperature in the form of a contour, both ML models demonstrated higher accuracy in predicting the average temperature of the heater as opposed to predicting the maximum temperature. It was presumed that each ML model was trained with the objective of enhancing the overall temperature prediction accuracy for the entire contour, rather than solely focusing on improving the accuracy of the specific pixel representing the maximum temperature.

Nevertheless, as evident from the 3D plot shown in Fig. 11(c), even in cases with a MAPE of 4.43% for the maximum temperature, the models were still capable of predicting the temperature distribution with remarkable accuracy. The performance comparison of ML models for the contour form is summarized in Fig. 12. Notably, in the case of the contour form prediction, where temperature is predicted according to location, the Multimodal ML model, which incorporates image data, exhibited superior accuracy compared to the traditional MLP model for both average temperature and maximum temperature predictions.

4. Conclusions

This study aimed to evaluate and compare the thermal prediction performance of multiphase flow in micro-pin fin arrays using various ML algorithms. All 155 data points collected under different operating conditions were utilized for learning, and two fabricated samples were selected for analysis. To examine the impact of each data modality, the values to be predicted were categorized into scalar and contour types, enabling a comprehensive accuracy comparison. Four ML algorithms, namely, XGBoost, LightGBM, MLP, and Multimodal ML, were employed for the prediction task, and their respective predictive accuracies were evaluated using MAPE. The key findings of the study are summarized below:

1. The accuracy of maximum heated surface temperature prediction in scalar form was 3.69%, 3.15%, 1.58%, and 2.47% in $MAPE_{avg}$ for XGBoost, LightGBM, MLP, and Multimodal ML, respectively. As for predicting the average heated surface temperature, $MAPE_{avg}$ was 4.17%, 3.43%, 1.64%, and 2.5% for XGBoost, LightGBM, MLP, and Multimodal ML, respectively. These results indicate that all models predicted the maximum temperature more accurately than the average temperature.
2. On the basis of the results, the MLP model showed the best accuracy in scalar temperature prediction. However, the accuracy of the Multimodal model was lower, which was likely due to the inclusion of spatial information from images. This inclusion introduced insignificant information for scalar-type prediction, despite the positive influence of flow patterns on temperature prediction.
3. The accuracy of maximum heated surface temperature prediction in contour form was 2.54% and 1.81% in $MAPE_{avg}$ for MLP and Multimodal ML. In addition, the $MAPE_{avg}$ of average heated surface temperature prediction was 1.77% and 0.84%, respectively, and all models predicted the average temperature more accurately than the maximum temperature.
4. The Multimodal method excels at predicting temperatures with spatial information, outperforming traditional decision tree-based algorithms and MLP. This feature is particularly important for designing embedded cooling solutions in electronic components susceptible to hot spots. Our methodology allows the prediction of temperature contours within micro-pin fin arrays during two-phase flow, aiding in the strategic placement of pin fins near hot spots and the design of heat sinks to reduce pressure loss. By enabling the estimation of temperature distributions without experimental data, our approach significantly aids in devising optimal cooling system designs for realizing efficient cooling systems.

CRediT authorship contribution statement

Haeun Lee: Data curation, Formal analysis, Investigation, Writing – original draft. **Geonhee Lee:** Data curation, Formal analysis, Writing – original draft. **Kiwan Kim:** Data curation, Methodology. **Daeyoung Kong:** Methodology, Writing – review & editing. **Hyoungsoon Lee:** Funding acquisition, Project administration, Supervision, Writing – review & editing.

Declaration of competing interest

The authors declare that they have no known competing financial interests or personal relationships that could have appeared to influence the work reported in this paper.

Data availability

Data will be made available on request.

Acknowledgments

This research was supported by the Challengeable Future Defense Technology Research and Development Program through the Agency for Defense Development (ADD) funded by the Defense Acquisition Program Administration (DAPA) in 2021 (No.915028201).

References

[1] M. Ciappa, Selected failure mechanisms of modern power modules, Microelectron. Reliab. 42 (4–5) (2002) 653–667.
[2] A. Vassighi, M. Sachdev, Thermal runaway in integrated circuits, IEEE Trans. Device Mater. Reliab. 6 (2) (2006) 300–305.
[3] W. Qu, I. Mudawar, Experimental and numerical study of pressure drop and heat transfer in a single-phase micro-channel heat sink, Int. J. Heat Mass Tran. 45 (12) (2002) 2549–2565.
[4] A. Koşar, Y. Peles, Thermal-hydraulic performance of MEMS-based pin fin heat sink, J. Heat Tran. 128 (2) (2006) 121–131.
[5] D. Kong, et al., A holistic approach to thermal-hydraulic design of 3D manifold microchannel heat sinks for energy-efficient cooling, Case Stud. Therm. Eng. 28 (2021) 101583.
[6] D. Kong, et al., Hierarchically structured laser-induced graphene for enhanced boiling on flexible substrates, ACS Appl. Mater. Interfaces 12 (33) (2020) 37784–37792.
[7] Y. Kim, et al., Heat transfer performance of water-based electrospray cooling, Int. Commun. Heat Mass Tran. 118 (2020) 104861.
[8] T.W. Wei, et al., Experimental and numerical investigation of direct liquid jet impinging cooling using 3D printed manifolds on lidded and lidless packages for 2.5D integrated systems, Appl. Therm. Eng. 164 (2020) 114535.
[9] T.E. Sarvey, et al., Embedded cooling technologies for densely integrated electronic systems, in: 2015 IEEE Custom Integrated Circuits Conference (CICC), IEEE, San Jose, CA, USA, 2015, pp. 1–8.
[10] C.H. Amon, et al., MEMS-enabled thermal management of high-heat-ux devices EDIFICE: embedded droplet impingement for integrated cooling of electronics, Exp. Therm. Fluid Sci. (2001) 12.
[11] D. Kong, et al., Single-phase thermal and hydraulic performance of embedded silicon micro-pin fin heat sinks using R245fa, Int. J. Heat Mass Tran. 141 (2019) 145–155.
[12] S. Krishnamurthy, Y. Peles, Flow boiling of water in a circular staggered micro-pin fin heat sink, Int. J. Heat Mass Tran. 51 (5–6) (2008) 1349–1364.
[13] A. Kosar, B. Schneider, Y. Peles, Two-phase flow across a bank of hydrofoil micro pin fins, in: 9th AIAA/ASME Joint Thermophysics and Heat Transfer Conference, American Institute of Aeronautics and Astronautics, San Francisco, California, 2006.
[14] A. Reeser, A. Bar-Cohen, G. Hetsroni, High quality flow boiling heat transfer and pressure drop in microgap pin fin arrays, Int. J. Heat Mass Tran. 78 (2014) 974–985.
[15] S. Krishnamurthy, Y. Peles, Flow boiling of water in a circular staggered micro-pin fin heat sink, Int. J. Heat Mass Tran. 51 (5–6) (2008) 1349–1364.
[16] A. Kawahara, P.M.-Y. Chung, M. Kawaji, Investigation of two-phase flow pattern, void fraction and pressure drop in a microchannel, Int. J. Multiphas. Flow 28 (9) (2002) 1411–1435.
[17] W. Qu, A. Siu-Ho, Experimental study of saturated flow boiling heat transfer in an array of staggered micro-pin-fins, Int. J. Heat Mass Tran. 52 (7–8) (2009) 1853–1863.
[18] J. Thibault, B.P.A. Grandjean, A neural network methodology for heat transfer data analysis, Int. J. Heat Mass Tran. 34 (1991) 2063–2070.
[19] Y. Qiu, et al., Machine learning algorithms to predict flow boiling pressure drop in mini/micro-channels based on universal consolidated data, Int. J. Heat Mass Tran. 178 (2021) 121607.
[20] L. Yang, Q. Wang, Y. Rao, Searching for irregular pin-fin shapes for high temperature applications using deep learning methods, Int. J. Therm. Sci. 161 (2021) 106746.
[21] H. Lee, et al., An artificial neural network model for predicting frictional pressure drop in micro-pin fin heat sink, Appl. Therm. Eng. 194 (2021) 117012.
[22] C.R. Kharangate, et al., Experimental investigation of embedded micro pin-fins for single-phase heat transfer and pressure drop, J. Electron. Packag. 140 (2) (2018) 021001.
[23] K. Kim, et al., A machine learning approach for predicting heat transfer characteristics in micro-pin fin heat sink, Int. J. Heat Mass Tran. (2022) (accepted).
[24] Y. Suh, R. Bostanabad, Y. Won, Deep learning predicts boiling heat transfer, Sci. Rep. 11 (1) (2021) 5622.
[25] F. Nie, et al., Image identification for two-phase flow patterns based on CNN algorithms, Int. J. Multiphas. Flow 152 (2022) 104067.
[26] Y. Zhang, et al., Two-phase flow regime identification based on the liquid-phase velocity information and machine learning, Exp. Fluid 61 (10) (2020) 212.
[27] D. Jung, et al., Thermal design and management of micro-pin fin heat sinks for energy-efficient three-dimensional stacked integrated circuits, Int. J. Heat Mass Tran. 175 (2021) 121192.
[28] C. Rubio-González, et al., Error propagation analysis for file systems, SIGPLAN NOTICES 44 (6) (2009) 270–280.
[29] H. Abdi, The Kendall rank correlation coefficient, Encyclopedia of Measurement and Statistics, Thousand Oaks, CA (2007) 508–510.
[30] T. Chen, C. Guestrin, "XGBoost: a scalable tree boosting system, in: Proceedings of the 22nd ACM SIGKDD International Conference on Knowledge Discovery and Data Mining, vol. 785, KDD'16), San Francisco, CA, 2016, p. 794.
[31] G. Ke, et al., LightGBM: a highly efficient gradient boosting decision tree, Adv. Neural Inf. Process. Syst. 30 (2017).
[32] J. Zhou, et al., Estimation of the TBM advance rate under hard rock conditions using XGBoost and Bayesian optimization, Undergr. Space 6 (5) (2021) 506–515.
[33] D.P. Kingma, J. Ba, Adam: A Method for Stochastic Optimization, 2017.
[34] J.C. Duchi, P.L. Bartlett, M.J. Wainwright, Randomized smoothing for (parallel) stochastic optimization, in: 2012 IEEE 51st IEEE Conference on Decision and Control (CDC), IEEE, 2012, pp. 5442–5444 Maui, HI, USA.
[35] T. Tieleman, G. Hinton, Lecture 6.5 - RMSProp, COURSERA: neural networks for machine learning. Lecture 9c: Using Noise as a Regularizer, 2012 Technical Reports.
[36] L. Ma, et al., Multimodal convolutional neural networks for matching image and sentence, in: 2015 IEEE International Conference on Computer Vision (ICCV), IEEE, Santiago, Chile, 2015, pp. 2623–2631.
[37] T. Baltrušaitis, C. Ahuja, L. Morency, Multimodal machine learning: a survey and taxonomy, IEEE Trans. Pattern Anal. Mach. Intell. 41 (2) (2019) 423–443, https://doi.org/10.1109/TPAMI.2018.2798607.
[38] P. Liashchynskyi, Grid search, random search, genetic algorithm: a big comparison for NAS, ArXiv Prepr. ArXiv1912.06059 (2019).
[39] S. Albawi, T.A. Mohammed, S. Al-Zawi, Understanding of a convolutional neural network, in: 2017 International Conference on Engineering and Technology, IEEE, 2017, pp. 1–6.